The haemodynamics of the human placenta in utero

***[a]Neele S. Dellschaft, *[a]George Hutchinson, *[a]Simon Shah, [b]Nia W. Jones, [a]Chris Bradley, [a]Lopa Leach, [d]Craig Platt, [a]Richard Bowtell, [a]Penny A. Gowland**

Sir Peter Mansfield Imaging Centre, Schools of [a]Physics and Astronomy, [b]Medicine and [c] Life Sciences, University of Nottingham

National Institute for Health Research (NIHR) Nottingham Biomedical Research Centre,

[d]Nottingham University Hospitals NHS Trust and University of Nottingham

*These authors contributed equally to this work

Submitted to PLOS Biology 7 August 2019

Resubmitted 30th January 2020

Address for correspondence: Penny Gowland; penny.gowland@nottingham.ac.uk

Abstract

We have used MRI to provide important new insights into the function of the human placenta *in utero*. We have measured slow net flow and high net oxygenation in the placenta *in vivo*, which is consistent with efficient delivery of oxygen from mother to fetus. Our experimental evidence substantiates previous hypotheses on the effects of spiral artery remodelling *in utero* and we have observed rapid venous drainage from the placenta, which is important since the outflow has been largely neglected in the past. Beyond Braxton Hicks contractions which involve the entire uterus, we have identified a new physiological phenomenon, the '*utero-placental pump*', by which the placenta and underlying uterine wall contracts independently of the rest of the uterus, expelling maternal blood from the intervillous space.

Main

The human placenta has a haemochorial circulation: maternal blood emerges from the spiral arteries of the uterine wall, to bathe villous trees containing fetal vessels (Figure 1a). This circulation is critical in fetal development, yet the patterns of maternal flow within the intervillous space (IVS) and details of venous return remain largely unknown. This circulation depends on the intrauterine environment and varies considerably between mammals and so ideally it should be investigated in humans *in utero* [1–3].

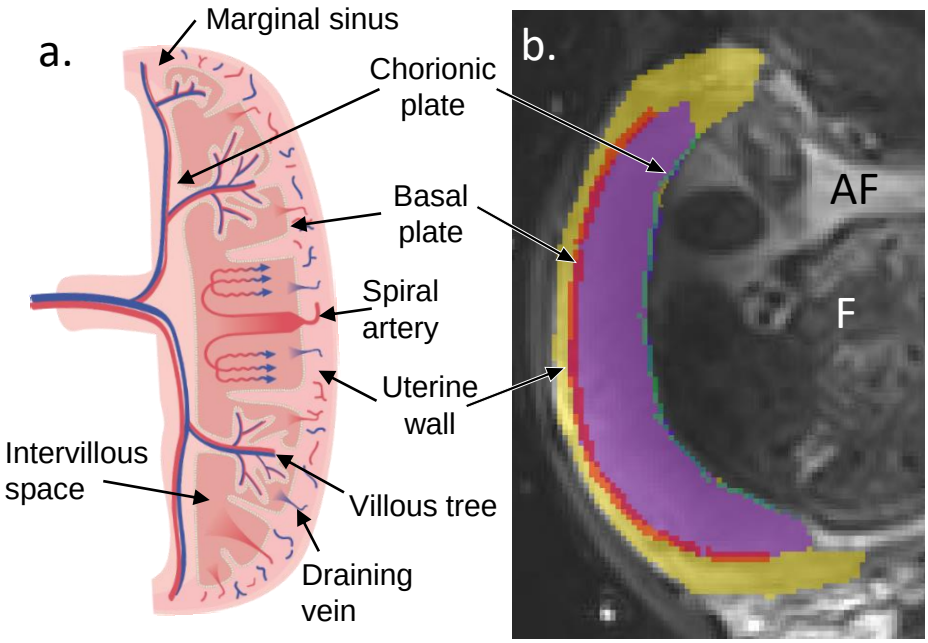

Figure 1: (a) **Schematic showing blood movement through the placenta.** Maternal blood enters the placenta via the spiral arteries, before percolating through the intervillous space (IVS) and then exiting through myometrial veins. Fetal blood flows through fetal vessels that cross the chorionic plate, before passing into stem villi (where fetal veins and arteries are closely apposed). Stem villi repeatedly branch to form the looped capillaries of the terminal villi, so that maternal and fetal blood supplies are in close proximity without mixing. (b) **Typical regions of interest used in the analysis shaded in colour on an MRI scan**; the purple area corresponding to the placental ROI with the fetus (F) and amniotic fluid (AF) also indicated.

Efficient oxygen extraction from maternal blood requires that the speed and pattern of blood flow within the IVS maintains a concentration gradient between the maternal and fetal circulations across the entire placenta at all times [4]. Fetal flow in the exchange region is slowed by distended capillary loops in the terminal branches of the villi, and spiral artery remodelling is thought to ensure relatively low pressure, low velocity, high volume maternal flow in the IVS [5]. However, the net velocity of flow across the IVS has not previously been measured, or linked to local movement within the IVS.

It is generally assumed that placental blood flow is in a steady state but recent mathematical modelling has suggested that active contraction of the stem villi (which have contractile elements along their length [6]) could assist maternal and fetal circulations in the placenta [7]. However, contractions of the placenta (independent of the rest of the uterus) have never been reported *in utero.*

Non-invasive imaging provides a unique opportunity to address these key unknowns. Ultrasound is a very powerful technique for guiding care in clinical obstetrics; uterine artery Doppler can measure flow in larger vessels and can assess spiral artery resistance indirectly [8], but provides limited information on movement of blood within or across the IVS [9]. Magnetic Resonance Imaging (MRI - glossary in Table S1) is increasingly used to study fetal growth and development, and diffusion weighted imaging (DWI) of the

utero-placental unit is established as a clinical marker of placental adhesion [10] and DWI and T_2^*-weighted imaging are increasingly being used to assess placental development [11–20].

Our aim was to provide new insights into blood movement and blood oxygenation in the human placenta using MRI. We have made the first measurements of the velocity of bulk movement through the placenta using Phase Contrast Angiography (PCA) MRI, and have compared this to smaller scale incoherent movements within the IVS and vascular network of the uterine wall, assessed using DWI. We used Quantitative Susceptibility Mapping (QSM) to assess placental oxygenation [21] and dynamic imaging to detect contraction of the placenta and its underlying uterine wall, independent of the rest of the uterus. We considered pre-eclamptic pregnancies as a model of altered placental function. Taken together these results provide detailed new insights into human placental haemodynamics.

Flow into and through the IVS

We measured net blood flow velocity using PCA which provides directional information by encoding net voxel velocity in the phase of the MRI signal [22]. Figure 2a shows maps of the three orthogonal components of velocity and net speed $|v|$, highlighting regularly spaced regions of relatively fast-moving blood (>0.1 cm/s) interspersed with regions of slow-moving blood (<0.05 cm/s). Quiver plots illustrate blood streaming from spiral arteries, percolating through the IVS and returning to the uterine veins, and resemble the 'fountains' predicted by mathematical models [23,24]. We often observed a small region of high velocity at the periphery of the placenta and broad regions of slow coherent movement near the chorionic plate (Fig. 2a). These patterns were stable over repeated measurements in the absence of gross movement (Fig. S1). For healthy control pregnancies (HC) the average net speed of flow was fastest in the uterine wall (see ROIs in Figure 1b), and slowed progressively through the vessels of the uterine wall and basal plate into the IVS (Fig. 2b, P=0.002 for net speed in uterine wall versus placenta). As expected, the velocity was higher in the independent fetal circulation of the chorionic plate. Figure 2d considers only voxels within the placenta in which the net velocity was high, and shows that velocities were similar for all three components in both forward and reverse directions for each subject. The flow measured in the placenta (<0.2 cm/s) was slower than predicted by some computational models (5 cm/s [24]), but supports others (0.6 cm/s [25]) and explains the long transit times previously measured with contrast-enhanced MRI [24] and arterial spin labelling [26]. It is also confirms the hypothesis that spiral artery remodelling in early pregnancy slows blood flow as it enters the IVS [27]. Figure 2e/f focuses on a strip of placenta adjacent to the uterine wall and shows that flows into and out of the placenta are of similar velocity and faster than flow parallel to the basal plate for HC (P=0.015 IN, P=0.050 OUT). This indicates that the speed of venous drainage, which is crucial for proper circulation in the IVS, is similar to that for arterial input.

Placentas from pre-eclamptic (PE) pregnancies (with or without fetal growth restriction) showed higher mean velocity (Fig. 2b, Table S3a, P<0.001) and wider range of velocities (Fig. 2d, Table S3b, averaging over all three components of velocity for each participant, P<0.001). This is consistent with incomplete spiral artery remodelling, and villous hypoplasia (histology for these subjects is given in Table S2a). Furthermore, the blood flow parallel and perpendicular to the basal plate was also faster in the PE pregnancies for which it could be measured (Figure 2e/f, PE faster than HC P<0.05 in every angular range). The blood also moved faster in the chorionic plate in the PE group (Fig. 2b, Table S3a, P<0.001), which may be due to changes in resistance of the fetal villous circulation caused by changes in fetal cardiac output [28] or altered villous branching and villous tone associated with pre-eclampsia related to altered angiogenic factors [29,30]. Histological confirmation of the placental anomalies is included where available and confirms maternal vascular malperfusion with villous hypoplasia and ischaemia (Table S2a).

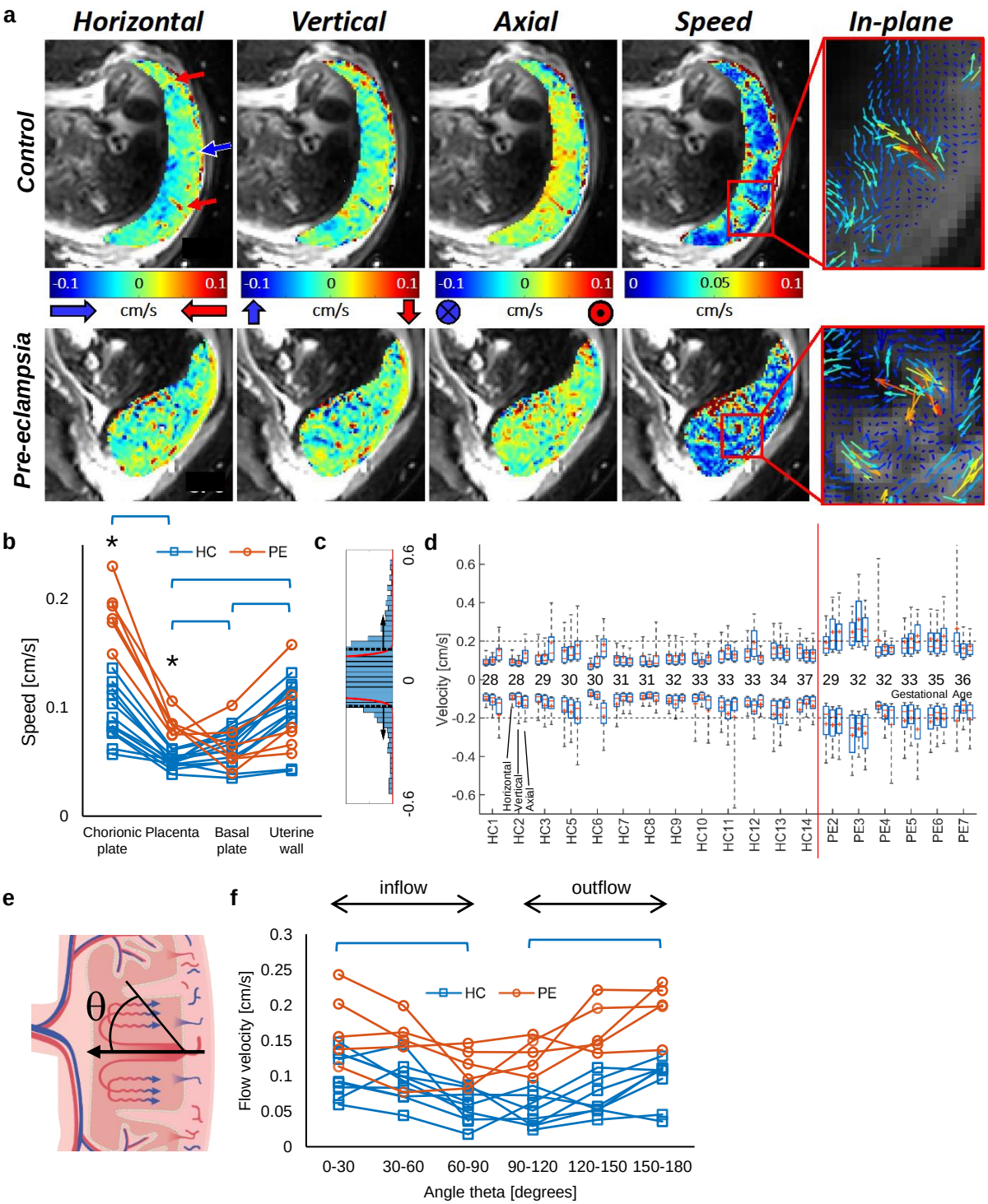

Figure 2: Net velocity of flow through the placenta. (a) Maps of velocity across the placenta for subjects HC3 (top) and PE6 (bottom) showing velocity in three orthogonal directions, net speed (|v|) and quiver plots that illustrate the direction and magnitude of blood flow within the imaging plane. (b) Speed of blood movement averaged across each ROI for each subject (* indicates significant difference between HC and PE, brackets indicate significant difference between ROIs for HC participants only; Table S3). (c) The distribution of one component of velocity across the placental ROI for one HC, magnified to illustrate the tails of the histogram. The red curve indicates a normal distribution fitted to data within one standard deviation of the full histogram, and the dashed lines indicate four standard deviations from the centre of that fitted peak; voxels beyond these dashed lines were identified as fast moving voxels. (d) The median (-), mean (+), interquartile range (box) and absolute range of the horizontal, vertical and axial velocity in these fast moving voxels. (e/f) The velocity of flow within the placenta in a narrow band adjacent to the basal plate, binned by direction of flow with respect to the normal to the basal plate, showing that the highest velocities are perpendicular to the basal plate for both inflow and outflow.

However, placental exchange depends not just on bulk movement, but also on smaller scale movement within the IVS, which we studied with diffusion weighted MR imaging (DWI). DWI is sensitive to any incoherent movement that cause variations in MRI signal phase across a voxel leading to attenuation of the net signal, but is not sensitive to coherent net flow. Figure 3a illustrates the change in DWI signal with increasing sensitivity to incoherent motion, defined by the diffusion weighting (*b*-value, in units of s/mm^2). The black and green lines indicate the expected effect of diffusion in stationary free water and blood due to restriction by cells [31]. The red bi-exponential curve includes a rapidly decaying component corresponding to the fraction of the voxel volume undergoing turbulent or shearing movement in the IVS or flowing through a randomly orientated vascular network in the uterine wall, and is characterised by the Intravoxel Incoherent Motion fraction (f_{IVIM} [32]). The blue line shows a non-linear decay that is slower than for f_{IVIM} (red line) but faster than for diffusion in blood (green line) and indicates random molecular displacements described by a non-Gaussian probability density function which can be characterized by kurtosis, *K* [33]. The kurtosis we observe in the placenta is much greater than that observed for restricted diffusion in the brain. This would be expected due to blood percolating through the IVS, (rather than restricted Brownian motion, which gives smaller values of *K* in neuroimaging). In reality, a voxel may contain many different types of motion, so we have modelled the data with this empirical equation:

$$S(b) = S_0(1 - f_{IVIM})e^{-bD+\frac{1}{6}b^2D^2K} + S_0 f_{IVIM} e^{-bD^*} \qquad [1]$$

where S_0 is the underlying MR signal, *b* is the diffusion weighting, *D* is the apparent diffusion coefficient and *D** is the pseudo-diffusion coefficient associated with f_{IVIM}.

Maps revealed that bands of high f_{IVIM} often coincided with, or were adjacent to regions where fast, coherently-moving blood entered the placenta (compare Figs. 3b and 2a and see Fig. 4c). These suggest that the pressure drop between the spiral arteries and IVS remains sufficient to propel jets of blood across almost the whole placental thickness. Bands of high f_{IVIM} were also observed corresponding to venous outflow from the placenta into the uterine wall. In the placenta of HCs regions of high *K* were generally distributed adjacent to focal regions of high f_{IVIM} (Fig. 3b), and f_{IVIM} decreased moving from the uterine wall to the basal plate and placental body (placenta versus uterine wall: P=0.001 for f_{IVIM}; Table S3a, Fig. 3c).

In PE, f_{IVIM} was reduced in the basal plate as previously reported [11,34] (P=0.046 and P=0.058 for basal plate and uterine wall), which could be the effect of the expected reduction in flow in those regions [27]. However, we found no significant change in f_{IVIM} within the placental body in PE, probably due to the counteracting effects of increased flow speed, reduced blood volume and altered villous density. A review and discussion of related literature is given in Table S4. There was a trend for *K* to be increased in PE placentas compared to HCs (P=0.058), and this was dominated by PE subjects also showing fetal growth restriction suggesting altered percolation through the IVS in this group where villous structure is expected to be altered [35]. However full interpretation of *K* requires quantitative histological comparisons.

The velocity and DWI datasets were acquired independently, but for six HC and six PE subjects the placental data could be overlaid. Fig. 3b shows the overlap of masks of the top 20th centile for values for $|v|$ (green), f_{IVIM} (red) or *K* (blue), and Fig. 3e summarizes the percentage of voxels lying in the overlap regions of these masks, averaged across subjects. Areas of high-speed blood flow streaming out of a spiral artery or into a vein were usually adjacent to areas of high incoherence (f_{IVIM}) and the area of overlap (yellow and white) was larger than expected by chance. This suggests that deceleration of fast coherent flow within the placenta drives the creation of eddies and retrograde shearing (see quiver plots in Fig. 2a and fountains predicted by mathematical models [23,24]) which will be critical for mixing in the IVS. Areas of high *K,* indicating driven percolation through the villous trees, showed low net speed (0.04 cm/s HC; 0.07 cm/s PE). These were less likely than expected to overlap with areas of high flow, suggesting high speed blood flows in cavities within the placental lobules as previously predicted [27]. The changes seen in PE suggest altered dissipation of the kinetic energy from the incoming blood, which could be used to investigate the relationship between high pressure flow and damage to villi in pre-eclampsia [27].

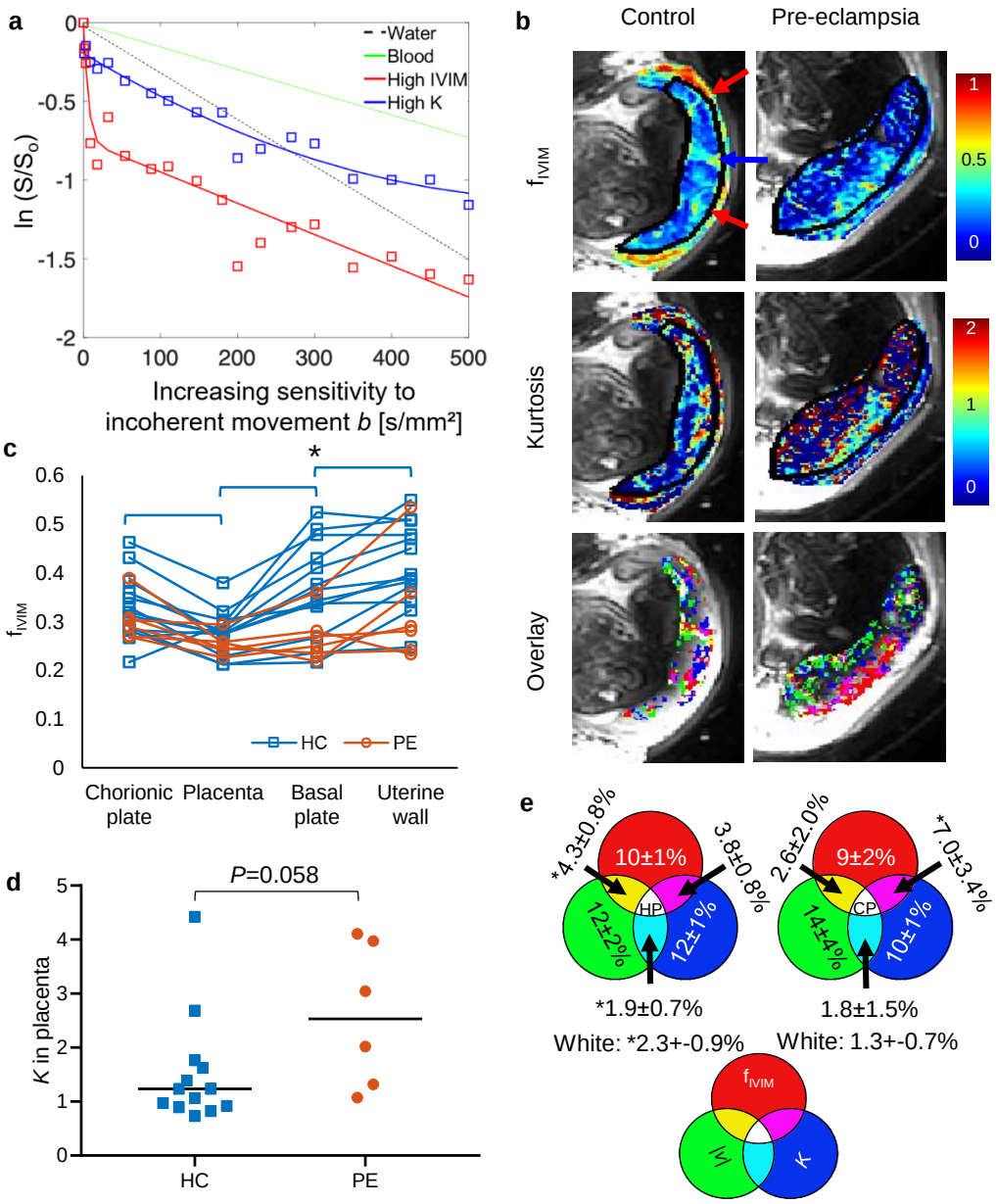

Figure 3: Incoherent flow in the placenta and its relationship to regions of high coherent flow. (a) Variation of signal with increasing sensitivity to incoherent movement (termed *b*-value in MRI). The black line shows the decay expected for unrestricted diffusion in stationary water. The green line illustrates slower decay typical of restricted diffusion by cells in blood samples [31]. The other curves show example placental data fitted to Equation 1. The red curve shows fast decay at low *b*-values caused by blood moving incoherently within a voxel, for instance due to turbulence. The blue curve shows faster decay than expected due to diffusion in static blood, suggesting that flow is causing some incoherent motion in the voxel; the curvature indicates non-Gaussian diffusion consistent with percolation through a porous medium. (b) Maps of f_{IVIM}, kurtosis and overlaid masks of voxels with highest 20% of values of f_{IVIM}, K or $|v|$ for HC3 and PE6. The red and blue arrows correspond to the arrows on Figure 2a. (c) Scatter plot showing average values of f_{IVIM} in the chorionic plate, placenta, basal plate and uterine wall regions of interest for each subject (asterisk indicates significant difference between HC and PE, Table S3). (d) Kurtosis in the placenta region for HC and PE. (e) Venn diagrams indicating top 20th centile of voxels in each primary ROI for both the HC and PE groups (mean ± standard deviation. *value differs from value expected by chanced by more than intersubject standard deviation.

Placental oxygenation

Magnetic susceptibility (χ) was measured to assess placental oxygenation. Figure 4a indicates that blood oxygenation is high in the IVS of HC, since for adult blood χ ranges from -0.1 ppm (fully oxygenated) to +3.4 ppm (fully deoxygenated [36]), with values below -0.1 ppm potentially indicating calcification, (the syncytium has $\chi \approx 0$). The maps capture the red blush of blood entering the intervillous space and blue strips

apparently corresponding to deoxygenated blood training through the IVS (see also Figure S6a&b). High blood oxygenation throughout the entire IVS is essential to maintain an oxygenation gradient between the maternal and fetal circulations. For PEs the average placental susceptibility was higher (more deoxygenated; *P*=0.010) but notably much more variable (Mann-Whitney, *P*=0.00002; Fig. 4b) than in HCs, suggesting that in PE deranged patterns of flow lead to variations in oxygen extraction across the placenta.

Figure 4c compares oxygenation, flow and T2* maps in a subject for whom all data could be overlaid. It shows areas of highly oxygenated blood flowing into the placenta and areas of less oxygenated blood flowing out of the placenta. It can be seen that T_2* and χ maps are similar but not identical. χ provides a more direct assessment of blood oxygenation than T2*, since T2* is also affected by the local spatial distribution of oxygenated blood and potentially incoherent flow. Since T2* is sensitive to changes in both flow and oxygenation, it is expected to provide a sensitive marker of placental function. Here we found T2*, averaged across each placenta, varied with birth weight centile even within the HC group, and was significantly lower in PE than in HC, also indicating reduced and more variable oxygenation (Figure 4d,Table S2a, Table S3b; Mann-Whitney, *P*=0.00016).

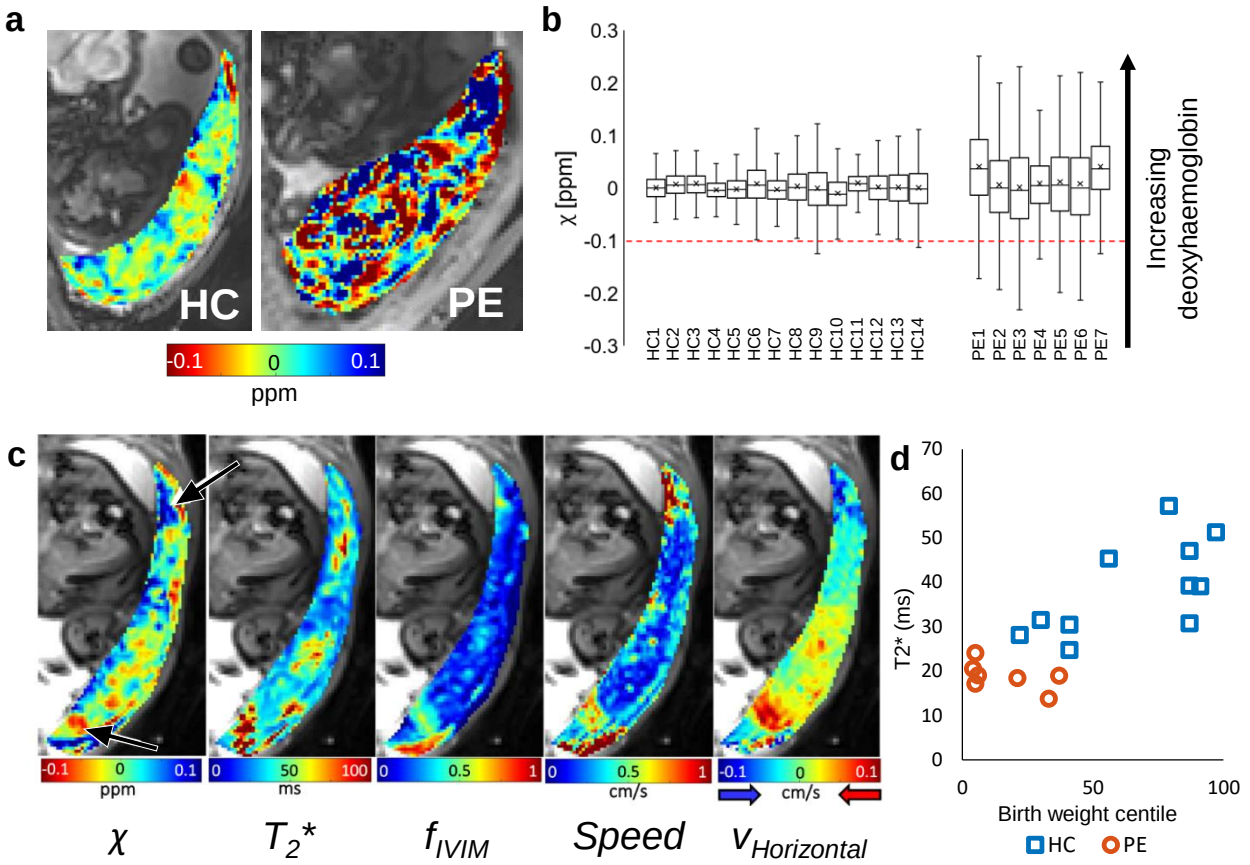

Figure 4: Magnetic susceptibility of the placenta (a) Maps of magnetic susceptibility (χ) of the placenta (blue corresponds to deoxygenated blood) for HC3 (moved slightly since the acquisition in Fig. 2a) and PE6. (b) Plot of the median (-), mean (+), interquartile range (box) and absolute range of susceptibilities (χ) for the HCs and PEs. The red dotted line indicates the value expected for fully oxygenated blood. The χ of the PE placentas is significantly higher (*P*=0.010). (c) Maps of χ, T_2*, f_{IVIM}, net speed and horizontal velocity for HC8. The lower arrow indicates oxygenated blood flowing into the placenta and the upper arrow indicates deoxygenated blood flowing out of the placenta (which was also associated with a reduced T2*). (d) Variation of T2* with birth weight centile.

The uteroplacental pump

Sub-clinical uterine contractions have recently been reported in MRI [37] and we have occasionally observed these ourselves (Fig. S3c+d). However more frequently we have observed orchestrated contractions of just the placenta and the underlying uterine wall, leading to transient reductions in placental volume (Fig. 5a and videos in Fig. S3a+b). We have termed this the '*uteroplacental pump'*. We observed one or more of these contractions over a 10-minute period in 12 out of 34 HCs and 7 out of 10 PEs with only three women reporting feeling any tightening when questioned immediately after the scan (Table S2a). These contractions involved a reduction in the area and thickening of the myometrium underlying (covered by) the placenta, a stretching or expansion of the rest of the uterine wall, and a simultaneous reduction in placental volume by up to 40% (Fig. 5b). The contractions varied in strength and duration (Fig. 5c) and caused the placenta to become thicker with less flat edges, and to appear darker and more heterogeneous on T_2*-weighted images, with dark bands in T_2* corresponding to bright bands on the susceptibility maps. These were different to changes seen with Braxton Hicks contractions, characterised by contraction of the entire uterine wall without alteration in placental volume (Fig. S3e). With the data available, we could not detect significant differences between the contractions in HC and PE pregnancies, but to confirm this we need to scan for longer to be able to monitor changes in the placenta before and after the contraction more frequently, possibly also using information from electrophysiology [38]. Some placental dysfunction is associated with factors that can increase placental thickness such as placental hyperinflation [39], enlargement by blood [40] or by chorioangiosis, maternal or fetal anaemia. Indeed we observed that the PE placentas were relatively thicker than the HC placentas (Table S2a and Figure S2, P=0.0481). However, we would not expect these factors to be transient or associated with changes in area of the myometrium underlying the placenta.

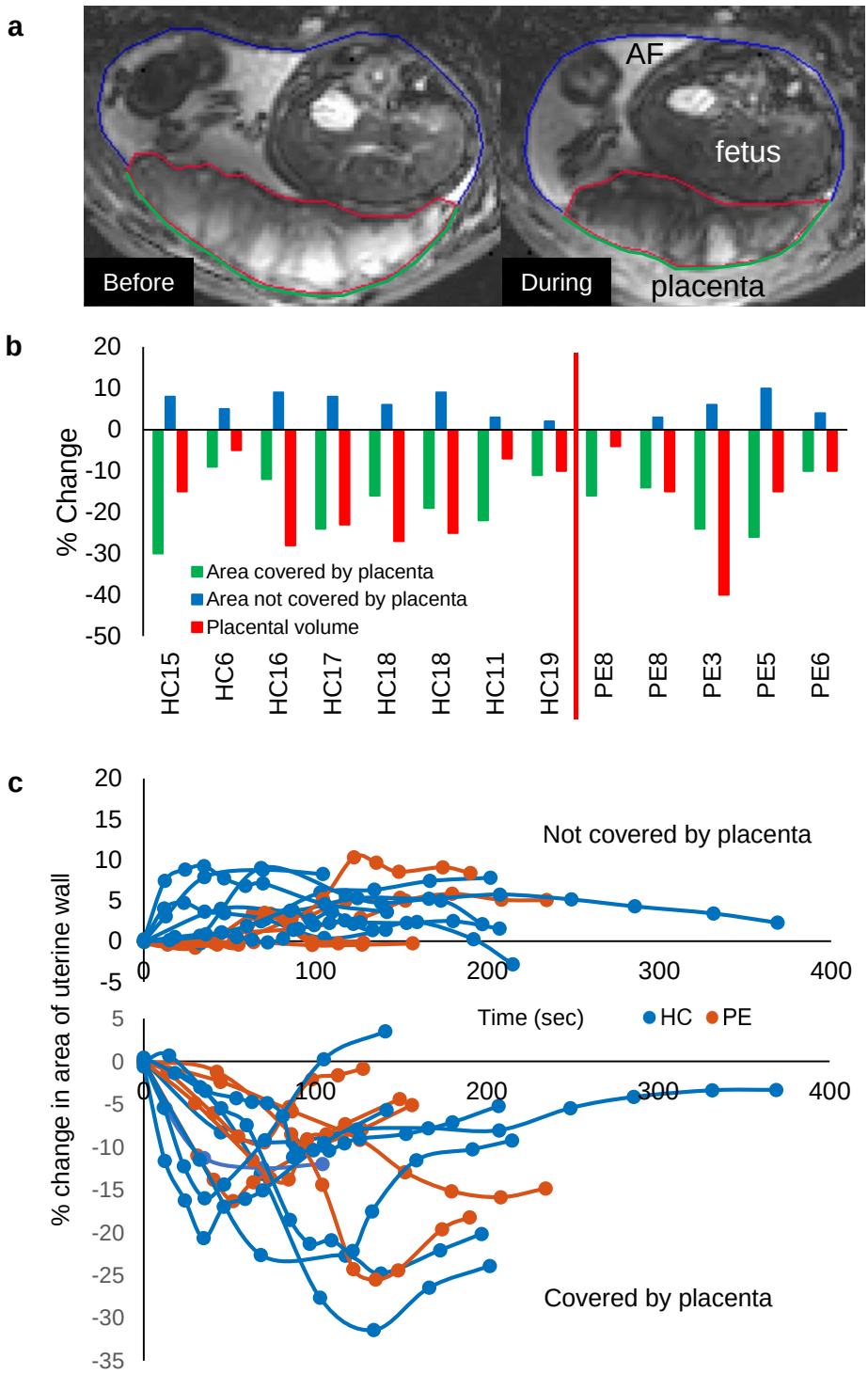

Figure 5: The uteroplacental pump. (a) T_2*-weighted images of the same placenta (HC17) before, and during a contraction, with lines indicating the placental ROI (red) and the parts of the uterine wall that are covered (green) and not covered by placenta (blue); AF indicates amniotic fluid. These images show a single slice, but data from slices across the whole uterus were summed to estimate the total volumes and areas involved. (b) Percentage change at maximum contraction of area of uterine wall covered by placenta, area of wall not covered by placenta and of placental volume (green, blue and red lines in (a) respectively), in each subject who had contractions during the 10-minute scan. Subjects HC18 and PE8 had two contractions in the ten minutes. Subjects are ordered by ascending gestational age at time of scan. (c) Time course of contractions in the same participants, with each line representing the change (%) of the wall not covered by placenta (increased during contraction) and the area of the uterine wall covered by placenta (decreased during contraction).

Discussion

We have performed a detailed experimental investigation of maternal placental haemodynamics *in utero*. In healthy pregnancies we found that the velocity of blood flow decreased from the uterine wall through to the placenta (Fig. 2, Table S3a), supporting the hypothesis that spiral artery remodelling reduces the velocity of blood flow as it enters the placenta [27]. We observed relatively fast flow into and out of the placenta (Fig. 2f) highlighting the importance of venous outflow which has received little attention in the past, but which is crucial for proper circulation in the IVS. Around the inflow jets we observed areas of high f_{IVIM} corresponding to turbulent mixing in the IVS, and between these areas we found non-Gaussian diffusion (high kurtosis), consistent with percolation through the IVS. We found relatively uniform, high oxygenation levels across the whole placenta, consistent with previous data that have shown that the difference in oxygen partial pressure between incoming (umbilical artery) fetal blood and the IVS is low (≈10mmHg [41] compared to ≈50mmHg in the lungs [42]), and the oxygen concentrations in the uterine artery and umbilical vein are similar[43]. These conditions of low oxygen extraction fraction suggest that relatively slow flow (low rate of delivery [44]) is required to ensure efficient oxygen transfer from the mother to the fetus. We have measured such slow net flow *in utero*.

We also studied pre-eclamptic (PE) pregnancies as a model of altered placental function. In such pregnancies, incomplete spiral artery remodelling has been predicted to lead to higher resistance to flow and thus faster flow through the IVS [27], which we observed. We also observed that this led to increased kurtosis in the placenta and altered patterns of blood movement, probably due to the combined effects of less efficient damping of the faster inflow, and altered villous density in PE [45]. The speed of movement of blood in the chorionic plate was also faster. Importantly, susceptibility (χ) measurements suggest this pattern of percolation led to lower and much more variable oxygenation across the placenta.

This study was not designed to investigate variation with gestational age, but we observed no change in flow or f_{IVIM} over the second or third trimester, in agreement with some previous studies [13,46] but contrary to others [16,47,48]. Little change in $|v|$ might be expected since both placental volume and uterine artery blood flow increase with gestation.

Most importantly, we have defined a new physiological phenomenon— the '*uteroplacental pump'*. This causes the periodic ejection of blood from the IVS but does not affect the fetal circulation since its entire blood volume is subject to the change in intrauterine pressure. This phenomenon may relate to previous reports that anchoring villi (connecting the chorionic plate to the uterine wall) are contractile, since such contractility would assist in maintaining the shape of the placenta as the wall contracts [7]. It may also be related to the myometrial–placental pacemaker zone that has recently been identified in rats [49]. It is likely that such uteroplacental contractions may have previously been identified as Braxton Hicks contractions involving the whole uterine wall (Fig. S3c), or localized uterine contractions on ultrasound [50] and MRI [50,51], which have been associated with transient reductions in both uterine blood flow [52] and placental oxygenation [37]. We agree with the previous contention that such contractions 'facilitate better blood flow through the placenta and the fetus' [53] and postulate that the uteroplacental pump is critical in avoiding the establishment of an unstirred layer limiting exchange near the villous surface [54]. Future work is needed to assess what happens to oxygenation and blood flow before, during and after the contraction, ideally measuring volume, oxygenation and flow changes simultaneously [55]. Identifying an ultrasound or electrophysiological signature [38] of the 'uteroplacental pump' should be a priority to accelerate research into this new phenomenon and probe its origin further. We also need to understand what triggers the contractions: is it a reduction in oxygenation, or an increase in pressure within the placenta? Are the contractions initiated in the myometrium of the placental bed [49] or by the anchoring villi [7]? The rate of detection of contractions was higher in PEs than HCs, but longer sampling in more subjects is required to be confident of any difference. The shape of the healthy placenta during a contraction is similar to the thickened shape of compromised placentas [56], raising the possibility that the pre-eclamptic placenta is permanently contracted to some extent.

Technical limitations

We characterised incoherent motion with a heuristic IVIM and kurtosis model [32,33], whereas the physical situation is a complex continuum, so the results will depend on the exact form of the experiment (Table S4) and a more data led approach to analysis [55] may be more appropriate. However the DWI sequence can also be designed to provide sensitivity to various types of motion (e.g. acceleration, circular motion, different length scales [57,58]). Such data could be used to inform and test physical models that will provide better insight into IVS movement and allow us to separate the effects of speed and volume of inflowing blood and villous density. This could then be used to tune the DWI sequence to provide specific markers of spiral artery transformation or placental porosity, which could provide new insights into placental function, and new biomarkers for investigating compromised pregnancies and response to therapies.

Any dephasing due to incoherent motion causes signal attenuation in the velocity measurements, which may bias results against flows with both coherent and incoherent contributions, and reduce maximum measured flows. Furthermore, the sensitivity of the velocity encoding sequence (<≈0.5 cm/s) had to be decided *a priori* which may have led to fast-flow being underestimated (Fig. 2e). In some PEs the signal in the placenta can be very low in places due to low oxygen, and *K* is not meaningful if *D* is very short due to infarcts. We excluded these regions from the analysis, which may have led us to underestimate the differences between HC and PEs.

The thickness of the placenta drops from 5.5 cm *in utero* [59] to 2.2 cm after delivery when much of the maternal blood is lost [60], suggesting that most of the volume *in utero* is made up of the maternal blood in the IVS. Therefore, we assume that MRI is mainly sensitive to blood movement in the IVS, since the voxels are too large to distinguish the counter flows in the fetal stem villi. However, sequences could be designed to separate these circulations, based on their different MR properties and scales of movement [55,61].

QSM is more directly related to tissue oxygenation than T2* but the exact relationship is not clear. If the placenta consisted only of adult blood a susceptibility of -0.1ppm would correspond to fully oxygenated blood and a susceptibility of +0.3ppm would correspond to a saturation of about 88% [36]. However, these values will overestimate the oxygenation of the maternal blood in the IVS for several reasons. First the placenta also contains villous tissue with a susceptibility of approximately zero. Secondly fetal blood has a sensitivity to oxygenation which is 75% of adult blood [62,63], although the fetal blood volume in the placenta is smaller and less oxygenated than the maternal blood. Compromised placentas can also include regions of haematoma containing haemoglobin degradation products (potentially more paramagnetic than deoxyhaemoglobin) and calcification (with more negative susceptibility).

We have no data on circulating angiogenic factors (e.g. PlGF) to confirm the diagnosis of pre-eclampsia. However, this is a well-characterised group of women (see Table S2a Demographics and Clinical Information worksheets). Histological diagnosis was possible in 50% of cases and confirmed maternal vascular malperfusion (MVM). Quantitative histological comparisons would have benefitted this study by assisting in separating different contributions to tissue magnetic susceptibility and in the interpretation of *K.*

Data quality was affected by maternal and fetal movement including uterine and placental contraction data. We over-acquired data to allow the selection of motion-free data sets, but alternative solutions are possible [55].

This work has provided new insights into placental blood flow and oxygenation, and the existence of the *uteroplacental pump*. Future work should investigate the link between oxygenation and flow during contractions, and effects of fetal and maternal cardiac pulsatility [9]. The results can be used to improve placental models (including *in vitro* models) and to optimize MRI pulse sequences to provide more specific information about placental abnormalities.

Methods

Demographics. Eligibility criteria for the study included age 18-45 years, body mass index (BMI) ≤30 kg/m^2, singleton pregnancy and no known fetal congenital anomalies. Patients were recruited for the study from Nottingham University Hospitals NHS Trust and written, informed consent was obtained from each subject. The study was approved by the East Midlands - Leicester Central Research Ethics Committee (16/EM/0308). We recruited 34 women with healthy pregnancies (Control, HC) and 13 women with pregnancies compromised by placental dysfunction (pre-eclampsia, PE, Table S2). In this group, pre-eclampsia was defined as blood pressure >140/90 mmHg on 2 separate occasions > 4 hours apart with proteinuria of >30 mg/mmol on a protein-creatinine ratio or 300mg in a 24 hour urine collection. Characteristics of the two groups are shown in Table S2a (Demographic and Clinical information worksheets). In the pre-eclampsia group all women required antenatal antihypertensive treatment with labetolol and a second agent was used in six cases. Seven of the eight women has significant proteinuria (PCR >30 mg/mmol) and the remaining patient had a BP of 171/110 prior to medication, raised transaminases (a diagnosis of PE based upon the International Society for the Study of Hypertension in Pregnancy (ISSHP) definition[64]) and histological confirmation of MVM. Six women with pre-eclampsia were in addition expecting a growth restricted baby less than the 10th centile [65] and all women required preterm delivery and there was one case of postnatal HELLP syndrome. Demographics were not different between HC and PE except for birth weight, birth weight centile and gestational age at birth (Table S2b). HC16 had a placental abruption resulting in the delivery of a baby with birth weight on the 50th centile, 3 weeks after the research scan. All subjects were analysed for contractions, but only a subset was analysed for blood flow in the placenta, due to changes in acquisition.

MRI. Scanning was performed on a Philips 3T Ingenia (Best, Netherlands) and women lay in the left or right decubitus position to avoid vena cava compression. The scanning session was split to allow the women to reposition after about 20 minutes. Posterior receive arrays that are built into the scanner bed were used along with an anterior abdominal array, positioned as close as possible to the placenta as determined from previous ultrasound, and repositioned after initial survey scans, if necessary. All scans were acquired in Normal Operating mode (whole body averaged SAR<2.0 W/kg). Severe RF inhomogeneity can occur in the pregnant abdomen at 3T and parallel transmission is not currently approved for use in pregnancy on this scanner. Therefore, the optimum flip angle was determined manually as that giving maximum signal within the placenta in a single-shot gradient echo, echo-planar imaging (EPI) image (range considered 90-150°). All data was acquired axially to the scanner to allow rapid planning, and scanning was respiratory-gated to minimise maternal motion.

Velocity-encoded phase maps (Phase Contrast Angiograms - PCA, Fig. 2) were reconstructed from the single-shot, respiratory-gated, pulsed gradient spin echo (PGSE) EPI sequence (Fig. S5, Table S5). The PGSE sequence was also used to produce DWI maps for IVIM and kurtosis analysis in the same planes (Fig. S5 and Table S5). When considering the literature it is important to note that the f_{IVIM} and K results (and to a lesser extent $|v|$) will depend on the exact details of the sequence used (Table S4).

For susceptibility mapping (Fig. 4), gradient echo images were acquired across the whole placenta, in the same orientation as the diffusion data, using a single-shot gradient echo EPI (TE was 35 ms for HC and 20 ms for PE to provide equivalent SNR in the maps given the shorter T_2* found in PE). Multiple single-shot EPI images were acquired (TE=20, 25, 30 and 35 ms) and fitted voxel-wise to a monoexponential decay to create T_2* maps (Fig. 4c)

Finally a single shot, respiratory gated, T_2*-weighted GRE EPI encompassing the whole uterus and placenta was acquired with respiratory gating at a minimum repetition rate of 9 s over a period of 10 minutes. After 2 or 4 minutes, oxygen was delivered to the mother to investigate its potential as an MRI contrast agent to assess transit times (results not reported).

After scanning women were asked to complete a questionnaire that recorded if they experienced any painful or non-painful contractions during the scan.

Data analysis. No automatic motion correction was applied because of the complexity of separate non-rigid maternal and fetal motion, and the large change in contrast through the data sets. Instead modulus

and phase datasets were inspected and volumes were removed from further analysis if they showed >5 mm displacement from the reference volume due to errors in respiratory gating, or where the boundary of the placenta was deformed due to fetal movement or a contraction. If more than 4 data points were discarded during the low *b*-values (b = 0 - 110 s/mm^2), or if more than 8 data points were discarded across the whole scan then the whole data set was removed.

Additionally, for the velocity-encoded data, the unwrapped phase was assessed for every slice and encoding direction, and if the unwrapped phase was corrupted due to fetal motion or maternal respiration, that data point was discarded. Net flow speed maps were only made for slices in which data were available for all velocity encoding directions. Note, the three velocity components shown in Figure 2a were measured independently. ROIs were drawn around the placenta, uterine wall, basal and chorionic plates on all slices on the b=0 s/mm^2 DWI images (Fig. 1b). Where possible, the same masks were then applied to the other DWI and velocity images, but if there had been movement the ROI was redrawn and in this case the datasets could not be subsequently overlaid (Fig. 3b&e).

The velocity encoding data was unwrapped by complex division of the encoded data by the unencoded data, and a high-pass Butterworth spatial filter (6 mm) was applied to data to remove global phase offsets due to respiration. Next, the blood flow velocity in each direction $v_{x,y,z}$ was calculated from:

$$v_{x,y,z} = \frac{\phi}{\gamma G_{x,y,z} T \Delta} \qquad [2]$$

where $G_{x,y,z}$ is the gradient amplitude in each of the orthogonal directions, Δ is the time between the start of each gradient lobe, T is the duration of gradient lobes (Fig. S5), and ϕ is the value of the unwrapped filtered phase. Colour maps for $v_{x,y,z}$ (which we have called horizontal, vertical and axial in the main text) along with the net speed maps, and quiver plots indicating the direction and amplitude of velocity projected onto the plane of the image were produced (Fig. 2a). The average speed in each ROI for each subject was found (Fig. 2b). Histograms of $v_{x,y,z}$ in the placenta were also created. The histograms did not show a Gaussian distribution, but their variance was calculated (σ^2) and voxels lying within $|v| < 1\sigma$ were fitted to a Gaussian distribution. Pixel values lying outside 4 standard deviations of this fitted distribution were then used to create box plots (Fig. 2d).

In some cases the placental signal was very low (particularly in PE) and so a threshold was applied to avoid fitting areas with little or no signal. To determine the threshold a close-to-zero signal region outside the subject and the mean of this ROI was taken as the noise level. Any pixel with signal less than 10 times the noise level at b = 0 would then be removed from further analysis, which was more likely to happen in PE where the T_2* was low.

To produce Figure 2f, the basal plate mask was eroded to one voxel wide and then approximated to series of lines by computing a convex hull. The angle between the in-plane velocity vector, and the angle normal to the basal plate was calculated for every voxel with in-plane speed >80th percentile, and within 5 voxels of these lines. The velocity was plotted against angle averaged across 30° bins (for clarity equal angular ranges were used, despite subtending varying solid angles). 1 PE and 1 HC participant could not be included as the shape of the basal plate was not suitable for computing a convex hull.

The DWI signals measured in each pixel at b-value, $S(b)$, for b≥88 s/mm^2 were fitted pixelwise to:

$$S(b) = S_0[e^{-bD}] \qquad [3]$$

to provide initial estimates of the apparent diffusion coefficient for water in tissue (D) and scaling factor S_0 in subsequent fits. Next the data was fitted to the following simple IVIM model (where the terms are as in Equation 1):

$$S(b) = S_0(1 - f_{IVIM})e^{-bD} + S_0 f_{IVIM} e^{-bD^*} \qquad [4]$$

The f_{IVIM}component was then subtracted from the data and the resulting data ($S'(b)$) was fitted to a model including kurtosis.

$$S'(b) = S_0(1 - f_{IVIM})e^{-bD+\frac{1}{6}b^2D^2K} \qquad [5]$$

where f_{IVIM} and S_0 are both fixed parameters using their values from the second fit (Equ 4.) and *K* is the kurtosis coefficient. The mean value in each ROI was calculated excluding voxels for which *D* was fitted as zero (< 10^{-7} mm^2/s, so that *K* is meaningless) or *K*=10 (maximum value allowed by fit, often corresponding to curves that suggested refocusing of signal from regions of rapid flow at some *b* values).

For subjects where there was minimal movement between the independent acquisition of the speed and f_{IVIM} /kurtosis data sets, pixels in the top 20th centile for speed, f_{IVIM} and kurtosis were mapped (Fig. 3b). The fraction of overlap between these three maps was calculated for each subject (Fig. 3b&e) and the mean values of the parameters in these mapped pixels was estimated (not shown).

Quantitative susceptibility maps (QSM). Phase images from the gradient echo data were masked to the uterus (mask drawn on magnitude images) and then unwrapped using a Laplacian based method [66] before performing a 2D V-SHARP filter [67,68] slice-by-slice to remove the background phase. Susceptibility maps were calculated using LSQR [21] using STI suite (https://people.eecs.berkeley.edu/~chunlei.liu/software.html; Fig. S6a). The average value of susceptibility (χ) within the placental ROI (on all slices) was estimated for each subject relative to the average value in an ROI of the amniotic fluid which is assumed to have $\chi = 0$ (ROI on 4 slices; care was taken to avoid areas in which amniotic fluid flow from fetal movements was obvious). Fig. S6b shows that the echo time has little effect on χ, and that the measurement is repeatable.

T2*. Modulus images from the EPI data were masked to the placenta for two echo times (TE1 and TE2). Average signal intensities were recorded and T2* calculated (Fig. 4d).

Uteroplacental Pump. N.S.D. identified subjects in whom she observed placental contractions during the 10 minute T_2*-weighted GRE EPI scan (movement within the placenta with a change in T_2*). Contractions were assessed by measuring the area of the entire uterine wall sectioned into a) covered by placenta and b) not covered by placenta, as well as total placental volume (Fig. 5a&b). Change of area and volume were calculated relative to stable baseline measurements before the start of the contraction. Since women were given oxygen during the acquisition to investigate its use as a method for measuring transit times, we noted whether the contraction started before or after the oxygen (Table S2a).

Statistics (Tables S2b and S3). All data was compared with non-parametric tests. When comparing HC and PE we used a Mann-Whitney test (continuous data) or chi square test (non-continuous data). Comparing between several ROIs we quote the *P* value for related-samples Friedman ANOVA (asymptotic significances) with Wilcoxon test (asymptotic, 2-tailed significances) showing a significant difference (*P*<0.05). The overlap regions were compared to expected values for chance overlap using a test for one mean.

Acknowledgment

Rubie-Jo Barker produced Figure 1a.

Author Contributions

P.A.G. and N.W.J. designed the study. N.W.J. recruited participants and collected clinical data. C.B., S.S. and N.S.D. collected MR data. P.A.G., S.S., N.S.D., R.B and G.H. analysed data. All authors interpreted results and wrote the manuscript.

Author Information

The authors have no competing interests. Correspondence and requests for materials should be addressed to P.A.G. (penny.gowland@nottingham.ac.uk).

Data availability

The datasets generated and analysed during the current study are available from the corresponding author on reasonable request.

Code availability

All code written for the current study is available on request.

References

1. Wilkening RB, Meschia G. Current topic: Comparative physiology of placental oxygen transport. Placenta. 1992;13(1):1–15.

2. Peter Kaufmann. Comparative Placentation: Guinea Pig. http://placentation.ucsd.edu/guinea.htm. 2004 [cited 2019 Jan 12].

3. Miglino MA, Carter AM, Ambrosio CE, Bonatelli M, De Oliveira MF, Dos Santos Ferraz RH, et al. Vascular Organization of the Hystricomorph Placenta: a Comparative Study in the Agouti, Capybara, Guinea Pig, Paca and Rock Cavy. Placenta. 2004;25(5):438–48.

4. McNanley T, Woods J. Placental Physiology. Glob Libr Women's Med. 2009;

5. Harris LK, Aplin JD. Vascular Remodeling and Extracellular Matrix Breakdown in the Uterine Spiral Arteries during Pregnancy. Reprod Sci. 2007;14(8_suppl):28–34.

6. Graf R, Schönfelder G, Mühlberger M, Gutsmann M. The perivascular contractile sheath of human placental stem villi: its isolation and characterization. Placenta. 1995;16(1):57–66.

7. Kato Y, Oyen ML, Burton GJ. Villous Tree Model with Active Contractions for Estimating Blood Flow Conditions in the Human Placenta. Open Biomed Eng J. 2017;11:36–48.

8. Cnossen JS, Morris RK, Ter Riet G, Mol BWJ, Van Der Post JAM, Coomarasamy A, et al. Use of uterine artery Doppler ultrasonography to predict pre-eclampsia and intrauterine growth restriction: A systematic review and bivariable meta-analysis. CMAJ. 2008;178(6):701–11.

9. Collins SL, Stevenson GN, Noble JA, Impey L. Developmental changes in spiral artery blood flow in the human placenta observed with colour Doppler ultrasonography. Placenta. 2012;33(10):782–7.

10. Cuthbert F, Teixidor Vinas M, Whitby E. The MRI features of placental adhesion disorder-a pictorial review. Br J Radiol. 2016;89(1065):20160284.

11. Moore RJ, Ong SS, Tyler DJ, Duckett R, Baker PN, Dunn WR, et al. Spiral artery blood volume in normal pregnancies and those compromised by pre-eclampsia. NMR Biomed. 2008;21(4):376–80.

12. Moore RJ, Strachan BK, Tyler DJ, Duncan KR, Baker PN, Worthington BS, et al. In utero perfusing fraction maps in normal and growth restricted pregnancy measured using IVIM echo-planar MRI. Placenta. 2000;21(7):726–32.

13. Derwig I, Lythgoe DJ, Barker GJ, Poon L, Gowland P, Yeung R, et al. Association of placental perfusion, as assessed by magnetic resonance imaging and uterine artery Doppler ultrasound, and its relationship to pregnancy outcome. Placenta. 2013;34(10):885–91.

14. Jakab A, Tuura RL, Kottke R, Ochsenbein-Kölble N, Natalucci G, Nguyen TD, et al. Microvascular perfusion of the placenta, developing fetal liver, and lungs assessed with intravoxel incoherent motion imaging. J Magn Reson Imaging. 2018;48(1):214–25.

15. Sohlberg S, Mulic-Lutvica A, Olovsson M, Weis J, Axelsson O, Wikstrom J, et al. Magnetic resonance imaging-estimated placental perfusion in fetal growth assessment. Ultrasound Obstet Gynecol. 2015;46(6):700–5.

16. Sohlberg S, Mulic-Lutvica A, Lindgren P, Ortiz-Nieto F, Wikström AK, Wikström J. Placental perfusion in normal pregnancy and early and late preeclampsia: A magnetic resonance imaging study.

Placenta. 2014;

17. Siauve N, Chalouhi GE, Deloison B, Alison M, Clement O, Ville Y, et al. Functional imaging of the human placenta with magnetic resonance. Am J Obstet Gynecol. 2015;213(4):S103–14.

18. Hutter J, Slator PJ, Jackson L, Gomes ADS, Ho A, Story L, et al. Multi-modal functional MRI to explore placental function over gestation. Magn Reson Med. 2019;81(2):1191–204.

19. Sinding M, Peters DA, Frokjaer JB, Christiansen OB, Petersen A, Uldbjerg N, et al. Prediction of low birth weight: Comparison of placental T2*estimated by MRI and uterine artery pulsatility index. Placenta. 2017;49:48–54.

20. Sørensen A, Hutter J, Seed M, Grant PE, Gowland P. T2* weighted placental MRI: basic research tool or an emerging clinical test of placental dysfunction? Ultrasound Obstet Gynecol. 2019;uog.20855.

21. Wang Y, Liu T. Quantitative susceptibility mapping (QSM): Decoding MRI data for a tissue magnetic biomarker. Magn Reson Med. 2015;73(1):82–101.

22. Gatehouse PD, Firmin DN, Collins S, Longmore DB. Real time blood flow imaging by spiral scan phase velocity mapping. Magn Reson Med. 1994;31(5):504–12.

23. Chernyavsky IL, Jensen OE, Leach L. A Mathematical Model of Intervillous Blood Flow in the Human Placentone. Placenta. 2010;31(1):44–52.

24. Lecarpentier E, Bhatt M, Bertin GI, Deloison B, Salomon LJ, Deloron P, et al. Computational Fluid Dynamic Simulations of Maternal Circulation: Wall Shear Stress in the Human Placenta and Its Biological Implications. PLoS One. 2016;11(1):e0147262.

25. Serov AS, Salafia CM, Brownbill P, Grebenkov DS, Filoche M. Optimal villi density for maximal oxygen uptake in the human placenta. J Theor Biol. 2015;364:383–96.

26. Shao X, Liu D, Martin T, Chanlaw T, Devaskar SU, Janzen C, et al. Measuring human placental blood flow with multidelay 3D GRASE pseudocontinuous arterial spin labeling at 3T. J Magn Reson Imaging. 2018;47(6):1667–76.

27. Burton GJ, Woods AW, Jauniaux E, Kingdom JCP. Rheological and Physiological Consequences of Conversion of the Maternal Spiral Arteries for Uteroplacental Blood Flow during Human Pregnancy. Placenta. 2009;30(6):473–82.

28. Crispi F, Comas M, Hernández-Andrade E, Eixarch E, Gómez O, Figueras F, et al. Does pre-eclampsia influence fetal cardiovascular function in early-onset intrauterine growth restriction? Ultrasound Obstet Gynecol. 2009;34(6):660–5.

29. Hendrix MLE, Palm KCM, Van Kuijk SMJ, Bekers O, Spaanderman MEA, Bons JAP, et al. Longitudinal changes in placental biomarkers in women with early versus late placental dysfunction. Hypertens Pregnancy. 2019;38(4):268–77.

30. Staff AC, Benton SJ, von Dadelszen P, Roberts JM, Taylor RN, Powers RW, et al. Redefining preeclampsia using placenta-derived biomarkers. Hypertension. 2013;61(5):932–42.

31. Funck C, Laun FB, Wetscherek A. Characterization of the diffusion coefficient of blood. Magn Reson Med. 2018;79(5):2752–8.

32. Le Bihan D, Breton E, Lallemand D, Aubin ML, Vignaud J, Laval-Jeantet M. Separation of diffusion and perfusion in intravoxel incoherent motion MR imaging. Radiology. 1988;168(2):497–505.

33. Jensen JH, Helpern JA, Ramani A, Lu H, Kaczynski K. Diffusional kurtosis imaging: the quantification of non-gaussian water diffusion by means of magnetic resonance imaging. Magn Reson Med. 2005;53(6):1432–40.

34. Derwig I, Akolekar R, Zelaya F, Gowland P, Barker GJ, Nicolaides K. Association of placental volume measured by MRI and birthweight percentile. J Magn Reson Imaging. 2013;34(5):1125–30.

35. Kingdom JC, Kaufmann P. Oxygen and placental villous development: origins of fetal hypoxia. Placenta. 1997;18(8):613–21 & 623–6.

36. Jain V, Abdulmalik O, Propert KJ, Wehrli FW. Investigating the magnetic susceptibility properties of fresh human blood for noninvasive oxygen saturation quantification. Magn Reson Med. 2012;68(3):863–7.

37. Sinding M, Peters DA, Frokjaer JB, Christiansen OB, Uldbjerg N, Sorensen A. Reduced placental oxygenation during subclinical uterine contractions as assessed by BOLD MRI. Placenta. 2016;39:16–20.

38. Lew S, Hämäläinen MS, Okada Y. Toward noninvasive monitoring of ongoing electrical activity of human uterus and fetal heart and brain. Clin Neurophysiol. 2017;128(12):2470–81.

39. Porat S, Fitzgerald B, Wright E, Keating S, Kingdom JCP. Placental hyperinflation and the risk of adverse perinatal outcome. Ultrasound Obstet Gynecol. 2013;42(3):315–21.

40. Alanjari A, Wright E, Keating S, Ryan G, Kingdom J. Prenatal diagnosis, clinical outcomes, and associated pathology in pregnancies complicated by massive subchorionic thrombohematoma (Breus' mole). Prenat Diagn. 2013;33(10):973–8.

41. Nye GA, Ingram E, Johnstone ED, Jensen OE, Schneider H, Lewis RM, et al. Human placental oxygenation in late gestation: experimental and theoretical approaches. J Physiol. 2018;596:5523–34.

42. Razi E, Nasiri O, Akbari H, Razi A. Correlation of arterial blood gas measurements with venous blood gas values in mechanically ventilated patients. Tanaffos. 2012;11(4):30–5.

43. Brandis K. The Physiology Viva: Questions and Answers. 2017. 252–256 p.

44. Schumacker PT, Cain SM. The concept of a critical oxygen delivery. Intensive Care Med. 1987;13(4):223–9.

45. Egbor M, Ansari T, Morris N, Green CJ, Sibbons PD. Morphometric placental villous and vascular abnormalities in early-and late-onset pre-eclampsia with and without fetal growth restriction. Br J Obstet Gynaecol. 2006;113(5):580–9.

46. Gowland PA, Francis ST, Duncan KR, Freeman AJ, Issa B, Moore RJ, et al. In vivo perfusion measurements in the human placenta using echo planar imaging at 0.5 T. Magn Reson Med. 1998;40(3):467–73.

47. Siauve N, Hayot PH, Deloison B, Chalouhi GE, Alison M, Balvay D, et al. Assessment of human placental perfusion by intravoxel incoherent motion MR imaging. J Matern Neonatal Med. 2019;32(2):293–300.

48. Jakab A, Tuura R, Kottke R, Kellenberger CJ, Scheer I. Intra-voxel incoherent motion MRI of the living human foetus: technique and test–retest repeatability. Eur Radiol Exp. 2017;1(1):26.

49. Lutton EJ, Lammers WJEP, James S, van den Berg HA, Blanks AM. Identification of uterine pacemaker regions at the myometrial-placental interface in the rat. J Physiol. 2018;596(14):2841–52.

50. Shiina Y, Ohnuki T. The role of asymmetric thickening of the uterine myometrium during pregnancy. Arch Gynecol Obstet. 2013;287(4):669–72.

51. Togashi K, Kawakami S, Kimura I, Asato R, Takakura K, Mori T, et al. Sustained uterine contractions: a cause of hypointense myometrial bulging. Radiology. 1993;187(3):707–10.

52. Oosterhof H, Dijkstra K, Aarnoudse JG. Uteroplacental Doppler Velocimetry during Braxton Hicks Contractions. Gynecol Obstet Invest. 1992;34(3):155–8.

53. Jacobson JD. Ultrasound, normal placenta - Braxton Hicks: MedlinePlus Medical Encyclopedia Image. https://medlineplus.gov/ency/imagepages/2254.htm. 2018.

54. Day PE, Cleal JK, Lofthouse EM, Hanson MA, Lewis RM. What factors determine placental glucose transfer kinetics? Placenta. 2013;34(10):953–8.

55. Slator PJ, Hutter J, Palombo M, Jackson LH, Ho A, Panagiotaki E, et al. Combined diffusion-relaxometry MRI to identify dysfunction in the human placenta. Magn Reson Med. 2019;82(1):95–106.

56. Damodaram M, Story L, Eixarch E, Patel A, McGuinness A, Allsop J, et al. Placental MRI in Intrauterine Fetal Growth Restriction. Placenta. 2010;31(6):491–8.

57. Paulsen JL, Özarslan E, Komlosh ME, Basser PJ, Song Y-Q. Detecting compartmental non-Gaussian diffusion with symmetrized double-PFG MRI. NMR Biomed. 2015;28(11):1550–6.

58. Turk EA, B G, Stout GN, Abulnaga S, Copeland N, Roberts D, et al. Assessment of placental microcirculation by joint analysis of flow compensated and nonflow compensated intravoxel incoherent motion data. https://index.mirasmart.com/ISMRM2019/PDFfiles/4068.html. In: Proc Int Soc Magn Res Med 27. 2019. p. 4068.

59. Miwa I, Sase M, Torii M, Sanai H, Nakamura Y, Ueda K. A thick placenta: a predictor of adverse pregnancy outcomes. Springerplus. 2014;3:353.

60. Baptiste-Roberts K, Salafia CM, Nicholson WK, Duggan A, Wang N-Y, Brancati FL. Maternal risk factors for abnormal placental growth: the national collaborative perinatal project. BMC Pregnancy Childbirth. 2008;8:44.

61. Melbourne A, Aughwane R, Sokolska M, Owen D, Kendall G, Flouri D, et al. Separating fetal and maternal placenta circulations using multiparametric MRI. Magn Reson Med. 2019;81(1):350–61.

62. Sun LQ, Macgowan CK, Portnoy S, Sled JG, Yoo SJ, Grosse-Wortmann L, et al. New advances in fetal cardiovascular magnetic resonance imaging for quantifying the distribution of blood flow and oxygen transport: Potential applications in fetal cardiovascular disease diagnosis and therapy. Echocardiogr J Cardiovasc Ultrasound Allied Tech. 2017;34(12):1799–803.

63. Portnoy S, Milligan N, Seed M, Sled JG, Macgowan CK. Human umbilical cord blood relaxation times and susceptibility at 3 T. Magn Reson Med. 2018;79(6):3194–206.

64. Brown MA, Magee LA, Kenny LC, Karumanchi SA, McCarthy FP, Saito S, et al. The hypertensive disorders of pregnancy: ISSHP classification, diagnosis & management recommendations for international practice. Vol. 13, Pregnancy Hypertension. Elsevier B.V.; 2018. p. 291–310.

65. Villar J, Papageorghiou AT, Pang R, Ohuma EO, Ismail LC, Barros FC, et al. The likeness of fetal growth and newborn size across non-isolated populations in the INTERGROWTH-21st project: The fetal growth longitudinal study and newborn cross-sectional study. Lancet Diabetes Endocrinol. 2014;2(10):781–92.

66. Schofield MA, Zhu Y. Fast phase unwrapping algorithm for interferometric applications. Opt Lett. 2003;28(14):1194–6.

67. Özbay PS, Deistung A, Feng X, Nanz D, Reichenbach JR, Schweser F. A comprehensive numerical analysis of background phase correction with V-SHARP. NMR Biomed. 2017;30(4):e3550.

68. Schweser F, Deistung A, Lehr BW, Reichenbach JR. Quantitative imaging of intrinsic magnetic tissue properties using MRI signal phase: An approach to in vivo brain iron metabolism? Neuroimage.

2011;54(4):2789–807.

69. Liu C. STI Suite. https://people.eecs.berkeley.edu/~chunlei.liu/software.html. Berkeley: UC Berkeley; 2017.

Table S1: Glossary

DWI	Diffusion weighted imaging: MRI scans that are sensitive to water diffusion but also small scale movements that are incoherent at the scale of an MRI voxel
IVIM	IntraVoxel Incoherent Motion: characterising the effect of incoherent motion (on a larger scale than diffusion) using DWI
Kurtosis	Description of non Gaussian diffusion used in MRI. In this context we believe it characterises driven percolation through the intervillous space
PCA	Phase contrast angiography: MRI scans in which the phase of the MRI signal is sensitized to velocity of any net movement of the content of the voxels (assuming equal signal contribution from all flow components)
Susceptibility χ	MRI measurements of the magnetic susceptibility of a tissue. This measure of the susceptibility of a material to being magnetisable and in this case it is directly related to the haemoglobin saturation and tissue oxygenation more generally (but can also be affected by tissue iron content, fat content and calcifications)
QSM	Quantitative Susceptibility Mapping: MRI measurements of the magnetic susceptibility of a tissue. This measure of the susceptibility of a material to being magnetisable and in this case it is directly related to the haemoglobin saturation and tissue oxygenation more generally (but can also be affected by tissue iron content, fat content and calcifications)
T2* weighted imaging	In this context MRI scans that are sensitive to the inhomogeneous distribution of deoxygenated blood and also to some extent changes in the tissue composition of the placenta
Voxel	The physical region within the human body from which the signal in each picture element (pixel) of the final MRI scan is obtained.

Table S2: Demographic and clinical information and blood flow and contraction results.

See Excel spreadsheets.

(a) Separate worksheets provide Demographic Information, Clinical Information for pre-eclamptic participants, and Contraction + Haemodynamic Results.

Clinical information includes blood pressure, mean arterial pressure, maximum urinary protein, 1st/2nd trimester placental biomarkers, placental histology, weight (centile) and feto-placental ratio (healthy controls had BP<135/80; two HCs had reduced PAPP-A (<0.415 MoM)), and contraction and blood flow data for each participant. Abbreviations: DM, data missing; S-VD, spontaneous labour, unassisted vaginal delivery; I-VD, induced labour, unassisted vaginal delivery; S-AVD, spontaneous labour, instrumental vaginal delivery; I-AVD, induced labour, instrumental vaginal delivery; EmCS, emergency Caesarean; ElCS, elective Caesarean; FGR, fetal growth restriction; PE, Pre-eclampsia; AB, abruption; D, diabetes; AN, anaemia; PI, pulsatility index; EDF, end diastolic flow; rev. EDF, reversed end diastolic flow; Asterisk in 'Contraction', 10 minute scan was DWI instead of EPI, not allowing detailed analysis of contraction; P, partial contraction (subtle); A, aspirin; L, labetalol; N, nifedipine; I, insulin; M, metformin; MS, magnesium sulphate given at delivery; PAPP-A, pregnancy-associated plasma protein A; MoM, multiple of median; MVM, maternal vascular malperfusion; occ., women reported occasional tightenings during the scan.

(b) Summary of demographic data. Pregnant women were either classed as healthy (control, HC) or pre-eclampsia (PE). All participants were assessed for contractions, but only a subset were assessed for blood flow (velocity, f_{IVIM} and K due changes in data acquisition). All data is given as median [IQR] and P-value for Mann-Whitney test except for parity, which is given as median [range] and P-value for chi square test.

b	*Blood flow cohort*			*Contraction cohort*		
	HC	PE	*P-value*	HC	PE	*P-value*
n	14	7		34	10	
Age, years	30 [5]	26 [17]	0.80	31 [7]	28 [12]	0.92
BMI, kg/m^2	24.4 [4.2]	29.3 [6.3]	0.11	24.8 [4.6]	26.6 [7.5]	0.45
Birth weight, kg	3.52 [0.86]	1.31 [0.70]	<0.0001	3.31 [0.94]	1.54 [0.88]	<0.0001
Birth weight centile, %	79 [47]	6 [28]	0.0002	63 [47]	14 [33]	0.0002
Gestational age at birth, weeks+days	38+5 [19d]	32+1 [33d]	<0.0001	38+3 [24d]	32+5 [38d]	<0.0001
Gestational age at MRI, weeks+days	31+2 [25d]	32+1 [44d]	0.54	32+0 [30d]	31+6 [45d]	0.82
Parity, n	0.5 [0-2]	0 [0-2]	0.92	0.5 [0-3]	0.5 [0-2]	0.81

Table S3: Consolidated results and statistical outcomes of (a) f_{IVIM}, *K*, velocity and *D* in each area; (b) average highest velocity (Fig. 2d) and susceptibility.

a		n	Chorionic plate	Placenta	Basal plate	Uterine wall	*P* Friedman	*P* Wilcoxon (if <0.05)
f_{IVIM}	HC	13	0.32 [0.09]	0.28 [0.05]	0.37 [0.15]	0.40 [0.14]	<0.001	0.013 (P v CP); 0.002 (CP v UW); 0.001 (P v BP); 0.004 (BP v UW); 0.001 (P v UW)
	PE	6	0.30 [0.06]	0.25 [0.03]	0.26 [0.07]	0.29 [0.16]	0.122	
	P MW		0.41	0.18	0.046 (U=16)	0.058		
K	HC	13	1.49 [1.60]	1.23 [0.80]	1.42 [1.15]	1.59 [1.07]	0.016	0.006 (P v BP); 0.003 (P v UW)
	PE	6	2.65 [3.04]	2.53 [2.75]	1.99 [2.14]	1.61 [0.91]	0.014	0.028 (CP v UW); 0.028 (BP v CP)
	P MW		0.11	0.058	0.64	0.83		
Velocity [cm/s]	HC	13	0.08 [0.04]	0.05 [0.01]	0.06 [0.02]	0.10 [0.03]	<0.001	0.013 (P v BP); 0.001 (BP v UW); 0.002 (P v UW); 0.001 (CP v P); 0.006 (CP v BP)
	PE	6	0.19 [0.03]	0.08 [0.02]	0.06 [0.03]	0.08 [0.06]	0.010	0.028 (BP v UW); 0.028 (CP v P); 0.028 (CP v BP); 0.046 (CP v UW)
	P MW		<0.001 (U=0)	<0.001 (U=0)	0.90	0.42		
D [$x10^{-3}$ mm^2/s]	HC	13	2.1 [0.7]	2.0 [0.4]	2.0 [0.6]	2.2 [0.6]	0.021	0.004 (P v UW); 0.026 (BP v UW)
	PE	9	1.9 [0.8]	1.8 [0.7]	2.0 [0.4]	2.0 [0.7]	0.22	
	P MW		0.42	0.64	0.64	0.90		

b		n	Placenta
Highest velocity [cm/s]	HC	13	0.13 [0.04]
	PE	9	0.21 [0.04]
	P MW		*<0.001 (U=0)*
Susceptibility [$x10^{-3}$ ppm]	HC	14	11 [97]
	PE	7	89 [347]
	P MW		*0.010 (U=15)*
T2* (ms)	HC	11	39.1 [16.6]
	PE	7	19.0 [3.4]
	P MW		*<0.001 (U=0)*

Pregnant women were either healthy (HC) or had pre-eclampsia (PE). All data are median [inter-quartile range]. Abbreviations: MW, Mann-Whitney; Friedman, related-samples Friedman ANOVA, between regions; CP, chorionic plate; P, placenta; BP, basal plate; UW, uterine wall.

Table S4: Review of f_{IVIM} measurements in the uteroplacental unit in compromised pregnancies. This table reviews all papers considering the effect of compromised pregnancy on f_{IVIM} (neglecting papers studying apparent diffusion coefficient alone or twin pregnancies). It shows that the literature on the effect of pregnancy compromise on f_{IVIM} is mixed. There are likely to be several explanations for this. First, the regions of interest interrogated have varied. Early papers found changes in the uterine wall and basal plate region rather than the fetal side of the placenta, which agrees with this study. The later papers have considered a placental ROI but it is hard to know if they have excluded the basal plate (and uterine wall) from this ROI and in some cases they seem to have explicitly included it. Secondly, the types of pregnancy compromise have varied with the studies that found a difference being more likely to have included FGR (though the numbers are low). Finally, the IVIM signal is sensitive to incoherent motion within a voxel. This will depend on the voxel size and also the exact sequence timing that we have summarized with TE below.

Source	b values [s/mm^2]	Other parameters if available	Demographics	ROI	Variation in f_{IVIM}
Moore et al 2000[9]	0, 0.2, 3, 15, 47, 80, 115, 206, 246, 346, 468	0.5T TE = 115 ms 3.5x2.5 mm SL = 7 mm	13 HC and 7 IUGR based on individualised birthweight	Outer zone probably included basal plate based on images.	Reduced in outer zone for IUGR (not significant in inner zone).
Moore et al 2008[8]	0–452	0.5T TE> 80 ms 3.5x2.5 mm SL = 7 mm	PE and IUGR based on individualized birthweight	Basal plate (placenta not considered)	Reduced in basal plate for PE rather than IUGR
Derwig et al 2013[10]	0, 0.7, 3, 9, 18, 32,54, 88, 147, 252, 500	1.5T, TE = 69 ms 3.75x3.75 mm SL = 4 mm	14 HC + 23 SGA; 24-29 weeks.	Basal plate and placenta separately	Lower across basal plate for SGA. NS trend in central placental ROI.
Sohlberg et al 2014[13]	0, 200, 400, 600, 800	1.5T	22 HC and 16 PE; 22-41 weeks	Placenta probably included Basal Plate ('as large a region as possible').	f_{IVIM} decreased in placenta late PE, increased in early PE
Sohlberg et al 2015[12]	0, 200, 400, 600 and 800	1.5T, SL = 6 mm Excluded areas of signal loss and poor fit.	22 HC and 13 PE/IUGR < 34 weeks. Placenta ROI not shown	Placenta (includes some basal plate from figures)	Significant difference between controls and IUGR or PE or both.
Jakab et al 2017[11]	0, 10, 20, 30, 40, 60, 80, 100, 150, 200, 300, 400, 500, 600, 700, 800, 900	1.5T and 3T TE = 75 ms 2x2 mm SL = 3-4 mm	N=33, 17-36 weeks, all had abnormalities.	Placenta and basal plate joint ROI based on images.	No change in compromised group, apparently separated on somatic abnormalities
Siauve et al 2019[14]	0, 15, 47, 80, 115, 206, 246, 346, 468, 700 and 1000	1.5T, TE = 87 ms (Small voxels as matrix is 256x256) SL=5 mm	N=55, <34 weeks, all awaiting termination for fetal abnormalities	Placenta (may include some of basal plate from figures)	Significantly lower in FGR

Abbreviations: T, Tesla; TE, echo time; SL, slice thickness; HC, healthy controls; SGA, small for gestational age fetus; PE, pre-eclampsia; ROI, region of interest; IUGR, intra-uterine growth restriction; FGR, fetal growth restriction.

Table S5: MR sequence parameters used in the acquisition of the IVIM and kurtosis, velocity and susceptibility/contraction data.

	IVIM and kurtosis diffusion	Velocity encoding	Susceptibility / for contraction data
Acquisition readout	Spin-echo	Spin-echo	Gradient-echo
TR / TE (ms/ms)	1800 / 61.4	1800 / 67.7	9000 / 35 (9000 / 20 for CP)
Resolution (mm^3, acq.)	2.5 x 2.5 x 6	2.5 x 2.5 x 6	2.4 x 2.4 x 4
FOV (mm^3)	400 x 400 x 54	400 x 400 x 54	400 x 400 x 200
Slices	5	5	50
Number of repeats	2	3	-
Gradient directions for PGSE	Oblique	x, y and z separately	
Diffusion-weighting (*b*-values, s/mm^2)	0, 1, 3, 9, 18, 32, 54 ,88, 110, 147, 180, 200, 230, 270, 300, 350, 400, 450, 500		
Venc (cm/s)		0 and ± 0.5	
Gradient amplitude G (mT/m)		0 and 21	
Gradient lobe length Δ (ms)	16	3.1	
Time between lobes *T* (ms)	31	34	
Scan duration (mins)	3	0.5	10 (one volume acquired every ~10 s)

Abbreviations: TR, repetition time; TE, echo time; acq., acquisition; FOV, filed of view; PGSE, pulsed gradient spin echo; Venc, velocity encoding.

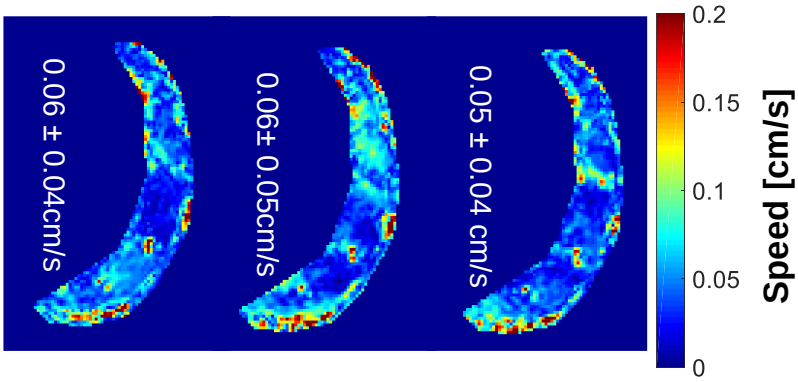

Figure S1: Net speed from HC3 from 3 repeated scans. The average net speed between the scans was 0.0577±0.005 cm/s.

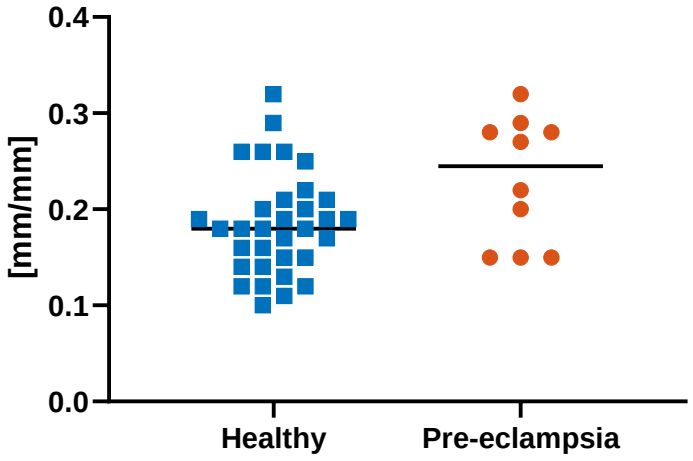

Figure S2: Thickness to length ratio measured for central slice of the placenta for the imaging slice showing largest area of placenta (*P*=0.048; Mann-Whitney test).

Fig S3a-d See separate video files.

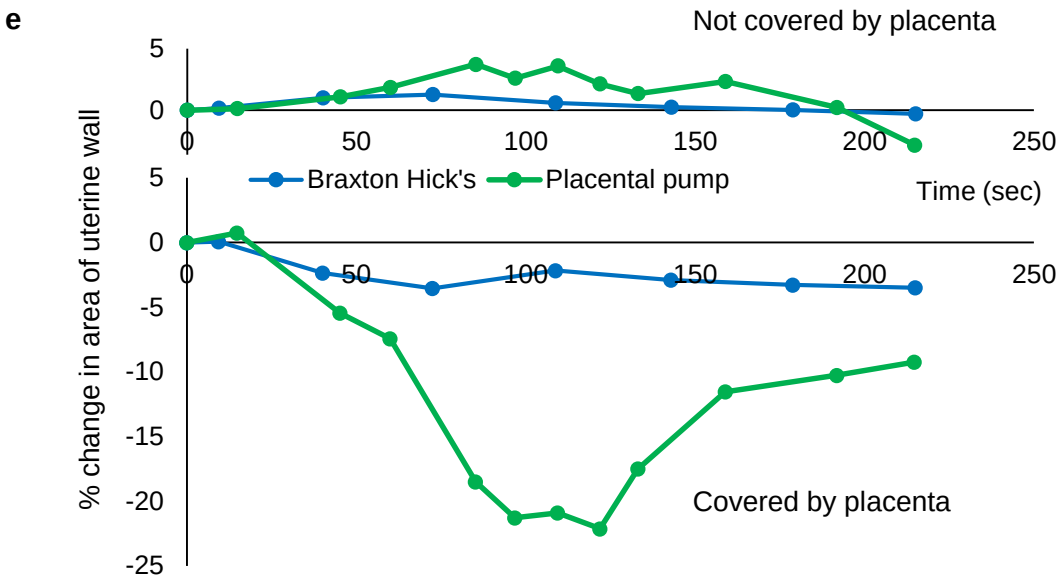

Figure S3: Placental pump compared to Braxton Hick's contraction.

Example time lapse videos for a placental pump contraction (with (a) and without (b) markings; HC11) compared to a Braxton Hick's contraction (with (c) and without (d) markings; HC29). (e) Time course of contractions in the same participants, with each line representing the change (%) of the wall not covered by placenta (increased during contraction) and the area of the uterine wall covered by placenta (decreased during contraction).

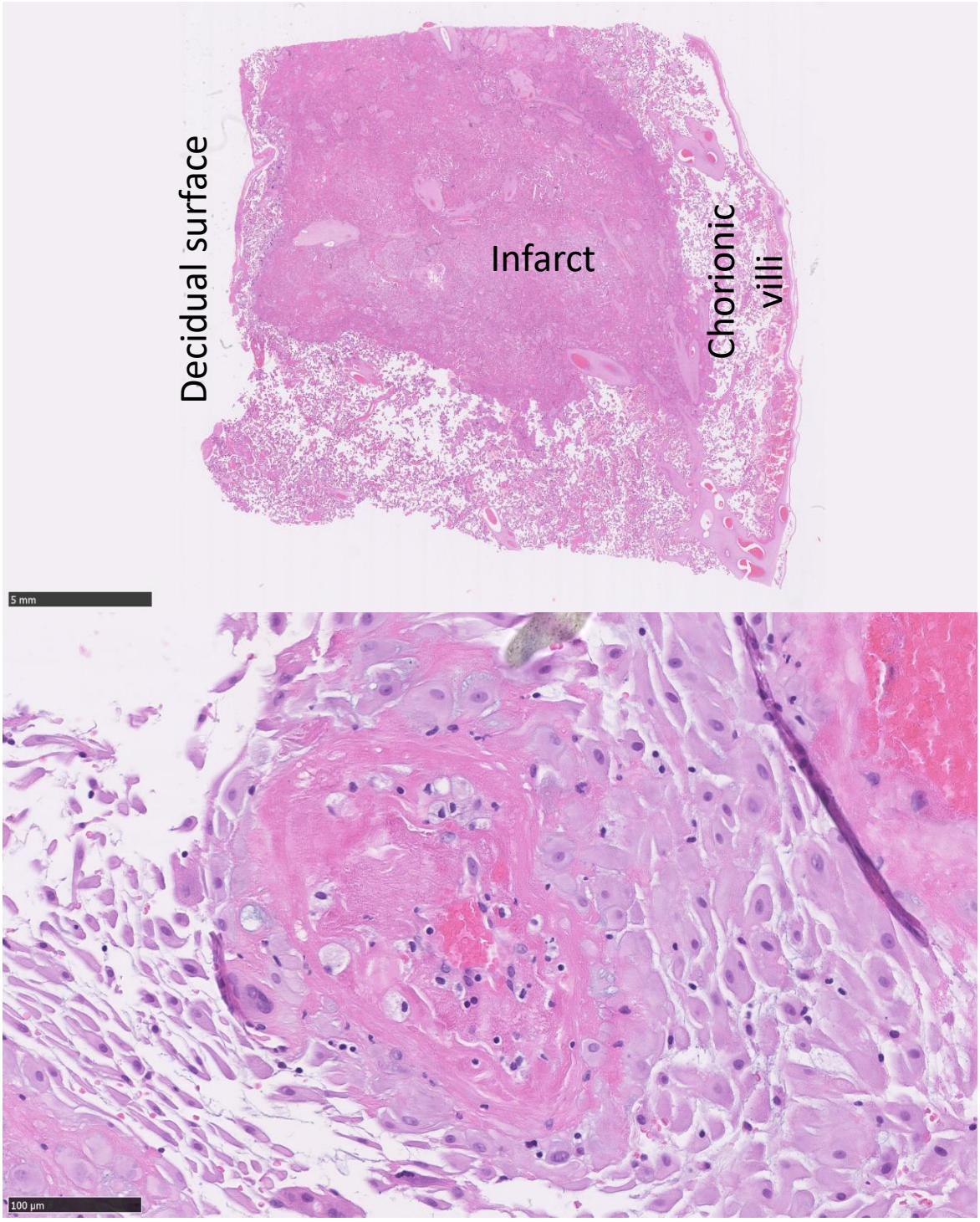

Figure S4: Histological examination of placenta (participant PE8). Haematoxylin and eosin staining from a placenta of a patient diagnosed with severe pre-eclampsia and HELLP syndrome and delivered by emergency Caesarean section at 28+6 weeks gestational age. A low resolution overview of the tissue (a, scale bar 5 mm) and a higher resolution magnification (b, scale bar 100 µm). This image demonstrates decidual arteriopathy including focal atherosis in keeping with a histological diagnosis of maternal vascular malperfusion. Placenta examined as per 'Tissue pathway for histopathological examination of the placenta' Royal College of Pathologists, 2017.

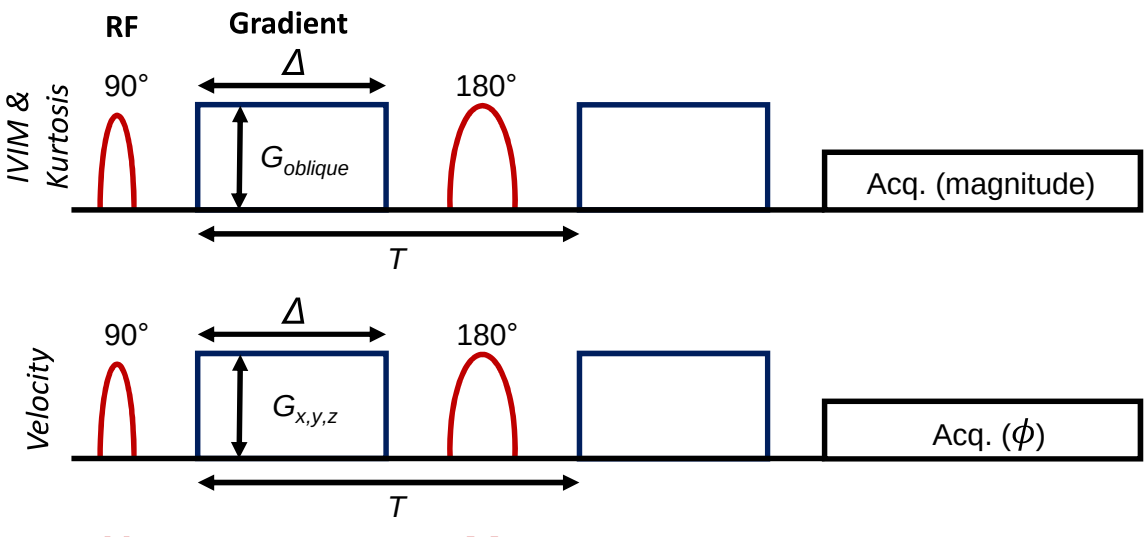

Figure S5: Pulsed Gradient Spin Echo (PGSE) sequence diagrams. IVIM and kurtosis: Δ, the duration of gradient lobes, and *T*, the time between the start of each gradient lobe, are fixed (see Table S3). The height of $G_{oblique}$ is increased to increase the b-value. After the second gradient, the magnitude of the MR signal is acquired. Velocity: Δ and *T* have different lengths compared to the IVIM and kurtosis acquisition (see Table S3). The gradient height is set to 21 mT/m for maximum velocity encoding of ±0.5 cm/s. After the second gradient, the MR phase signal (*Φ*) is reconstructed for velocity measurement.

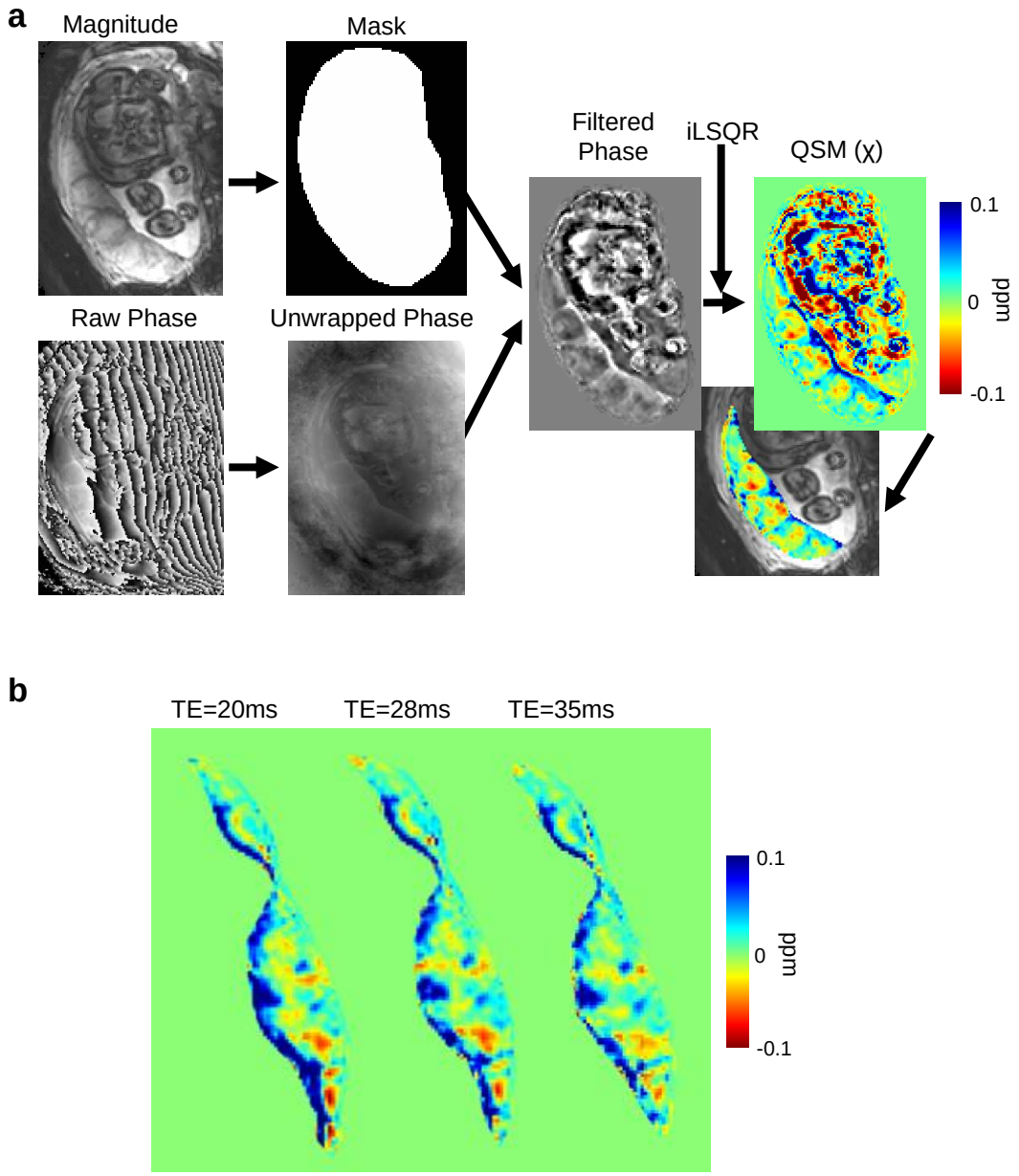

Figure S6: Pipeline for Quantitative Susceptibility Mapping (QSM). (a) First column: The raw magnitude and phase data acquired from the gradient echo acquisition (Table S3). Second column: The uterus is masked in the magnitude data, and phase images are unwrapped within that mask using a Laplacian based method. Third column: A 2D V-SHARP filter slice-by-slice to remove the background phase is applied to the unwrapped phase and subsequently the uterus mask is applied to make the filtered phase. Forth column: Susceptibility maps are calculated using LSQR [61]. (b) The χ calculated using the QSM pipeline for 3 different echo time (TE) values shows its general insensitivity to the echo time used in the gradient echo EPI acquisition.